

Exact spatial and temporal balance of energy exchanges within a horizontally explicit/vertically implicit non-hydrostatic atmosphere

David Lee^{a,*}, Artur Palha^b

^a*Bureau of Meteorology, Melbourne, Australia*

^b*Faculty of Aerospace Engineering, Delft University of Technology, Kluyverweg 2, 2629 HS Delft, The Netherlands*

Abstract

A new horizontally explicit/vertically implicit (HEVI) time splitting scheme for atmospheric modelling is introduced, for which the horizontal divergence terms are applied within the implicit vertical substep. When using a spatial and vertical temporal discretisation that preserve the skew-symmetric structure of the non-canonical Hamiltonian form of the equations of motion, this scheme allows for the exact balance of all energetic exchanges in space and time. However since the choice of mass flux for which this balance is satisfied is not consistent with the horizontal velocity at the end of the time level the scheme still admits a temporal energy conservation error. Linearised eigenvalue analysis shows that similar to a fully implicit method, the new HEVI scheme is neutrally stable for all buoyancy modes, and unlike a second order trapezoidal HEVI scheme is stable for all acoustic modes below a certain horizontal CFL number. The scheme is validated against standard test cases for both planetary and non-hydrostatic regimes. For the planetary scale baroclinic instability test case, the new formulation exhibits a secondary oscillation in the potential to kinetic energy power exchanges, with a temporal frequency approximately four times that exhibited by a horizontally third order, vertically second order trapezoidal scheme. For the non-hydrostatic test case, the vertical upwinding of the potential temperature diagnostic equation is shown to reduce spurious oscillations without altering the energetics of the solution, since this upwinding is performed in an energetically consistent manner.

Horizontally explicit/vertically implicit (HEVI) schemes are a popular approach to time stepping in atmospheric models. This is on account of the importance of negating the CFL limit imposed by the explicit representation of vertical dynamics, and the desire to avoid the computational expense of a three dimensional implicit solve at each nonlinear iteration. Numerous HEVI schemes have been implemented [1–5] in previous models. These schemes are typically motivated by a desire to improve upon the stability and dispersion properties of the second order trapezoidal HEVI scheme through the use of additional sub steps within each time step [6, 7]. The application of additional substeps qualitatively improves the stepping scheme by ensuring the linear stability of the horizontal buoyancy and acoustic models below some CFL limit.

In the present article a new HEVI scheme is introduced, motivated by a desire to preserve the exact balance of energetic exchanges. The scheme is implemented within the context of a mixed mimetic spectral element spatial discretisation [8] and energy conserving implicit vertical time stepping method [9] that together allow for the exact balance of all energy exchanges in space and time. This is achieved by evaluating the horizontal mass and temperature fluxes within the vertically implicit sub-step, after first computing a provisional horizontal velocity from which to derive a second order temporal representation of the horizontal fluxes. Unlike other HEVI schemes, the new method is composed of only two horizontal and one vertical substep. In contrast to the standard second order trapezoidal splitting scheme, linear analysis shows the new method to be unconditionally stable for all acoustic modes below some horizontal CFL number, and all buoyancy modes independent of CFL number. While the energetic exchanges are all exactly balanced, since the provisional horizontal velocity does not exactly match the final horizontal velocity at the end of the time step, the scheme admits a horizontal energy conservation error, as is the case for explicit schemes used to solve compressible flow problems.

*Corresponding author. Tel. +61 452 262 804.

Email address: davelee2804@gmail.com (David Lee)

The remainder of this article proceeds as follows. In section 1 the continuous 3D compressible Euler equations for atmospheric flows are introduced in variational form. The discrete analogue of these equations is then introduced in section 2, and the new HEVI splitting scheme is described in section 3. Section 4 describes the energetically consistent stabilisation of spurious oscillations in potential temperature via the upwinding of the corresponding test space. The reproduction of standard test cases is described in section 5. Finally the conclusions are discussed in section 6.

1. Skew-symmetric variational structure of the compressible Euler equations

The compressible Euler equations for atmospheric flows may be expressed in skew-symmetric form for the evolution of the velocity, \mathbf{u} , density, ρ , and density weighted potential temperature, Θ , as:

$$\frac{\partial \mathbf{u}}{\partial t} = -\mathbf{q} \times \mathbf{U} - \nabla \Phi - \theta \nabla \Pi \quad (1a)$$

$$\frac{\partial \rho}{\partial t} = -\nabla \cdot \mathbf{U} \quad (1b)$$

$$\frac{\partial \Theta}{\partial t} = -\nabla \cdot (\theta \mathbf{U}) \quad (1c)$$

where $\mathbf{q} := (\nabla \times \mathbf{u} + f)/\rho$ is the potential vorticity (and f is the Coriolis term), $\mathbf{U} := \rho \mathbf{u}$ is the mas flux, $\Phi := \frac{1}{2} \mathbf{u} \cdot \mathbf{u} + \rho g z$ is the Bernoulli function (with g the gravitational acceleration and z the height), $\theta := \Theta/\rho$ is the potential temperature, and $\Pi := c_p (R\Theta/p_0)^{\frac{R}{c_v}}$ is the Exner pressure (where c_v and c_p are the specific heats at constant volume and temperature respectively). The corresponding Hamiltonian (total energy) is given as:

$$H = \int_{\Omega} \underbrace{\frac{1}{2} \rho \mathbf{u} \cdot \mathbf{u}}_K + \underbrace{\rho g z}_P + \underbrace{\frac{c_v}{c_p} \Theta \Pi}_{I} d\Omega, \quad (2)$$

where K is the kinetic energy, P is the potential energy, and I is the internal energy. The variational derivatives of the Hamiltonian with respect to the dependent variables $(\mathbf{u}, \rho, \Theta)$ are

$$\frac{\delta H}{\delta \mathbf{u}} = \rho \mathbf{u} =: \mathbf{U}, \quad (3a)$$

$$\frac{\delta H}{\delta \rho} = \frac{1}{2} \mathbf{u} \cdot \mathbf{u} + g z =: \Phi, \quad (3b)$$

$$\frac{\delta H}{\delta \Theta} = c_p \left(\frac{R\Theta}{p_0} \right)^{\frac{R}{c_v}} =: \Pi, \quad (3c)$$

give the mass flux, \mathbf{U} , the Bernoulli function, Φ and the Exner pressure, Π respectively.

The weak form of (1) is given for $\mathbf{u}, \mathbf{U} \in H(\text{div}, \Omega)$ and $\rho, \Theta, \Phi, \Pi \in L^2(\Omega)$ as:

$$\left\langle \boldsymbol{\beta}, \frac{\partial \mathbf{u}}{\partial t} \right\rangle = -\langle \boldsymbol{\beta}, \mathbf{q} \times \mathbf{U} \rangle + \langle \nabla \cdot \boldsymbol{\beta}, \Phi \rangle + \langle \nabla \cdot \mathbb{P}^{\text{div}} [\theta \boldsymbol{\beta}], \Pi \rangle, \quad \forall \boldsymbol{\beta} \in H(\text{div}, \Omega) \quad (4a)$$

$$\left\langle \gamma, \frac{\partial \rho}{\partial t} \right\rangle = -\langle \gamma, \nabla \cdot \mathbf{U} \rangle, \quad \forall \gamma \in L^2(\Omega) \quad (4b)$$

$$\left\langle \sigma, \frac{\partial \Theta}{\partial t} \right\rangle = -\langle \sigma, \nabla \cdot \mathbb{P}^{\text{div}} [\theta \mathbf{U}] \rangle, \quad \forall \sigma \in L^2(\Omega) \quad (4c)$$

where we have invoked inner product notation as $\langle a, b \rangle = \int_{\Omega} a b d\Omega$, the integration-by-parts relation $\langle \boldsymbol{\beta}, \nabla \alpha \rangle = -\langle \nabla \cdot \boldsymbol{\beta}, \alpha \rangle$ (assuming periodic or homogeneous boundary conditions) in (4), and introduced the L^2 projection to $H(\text{div}, \Omega)$

$$\mathbb{P}^{\text{div}} : [L^2(\Omega)]^3 \rightarrow H(\text{div}, \Omega). \quad (5)$$

Specifically, consider $\mathbf{v} \in [L^2(\Omega)]^3$ its projection $\mathbb{P}^{\text{div}}[\mathbf{v}] \in H(\text{div}, \Omega)$ is given by

$$\langle \mathbb{P}^{\text{div}}[\mathbf{v}], \boldsymbol{\beta} \rangle = \langle \mathbf{v}, \boldsymbol{\beta} \rangle, \quad \forall \boldsymbol{\beta} \in H(\text{div}, \Omega). \quad (6)$$

Energy conservation is assured for the choice of $\boldsymbol{\beta} = \mathbf{U}$, $\gamma = \Phi$, $\sigma = \Pi$ by summing all equations in (4), such that

$$\left\langle \frac{\delta H}{\delta \mathbf{u}}, \frac{\partial \mathbf{u}}{\partial t} \right\rangle + \left\langle \frac{\delta H}{\delta \rho}, \frac{\partial \rho}{\partial t} \right\rangle + \left\langle \frac{\delta H}{\delta \Theta}, \frac{\partial \Theta}{\partial t} \right\rangle = \frac{\partial H}{\partial t} = 0. \quad (7)$$

where the key ingredient for energy conservation is skew-symmetry of (4).

2. Discrete formulation

In this section the mixed mimetic spectral element spatial discretisation used in the model is briefly introduced. For the purposes of this article the salient feature of this method is that it allows for the preservation of the skew-symmetric structure of the compressible Euler equations, and thus the conservation of energy and energetic exchanges in the discrete form. For a more detailed discussion the reader is referred to previous work on the use of this method for geophysical flow modelling [8, 10, 11], as well as more foundational works on the subject [12–15]. In order to begin this discussion we introduce the finite dimensional subspaces $\mathcal{P}_h \subset H^1(\Omega)$, $\mathcal{W}_h \subset H(\text{curl}, \Omega)$, $\mathcal{U}_h \subset H(\text{div}, \Omega)$ and $\mathcal{Q} \subset L^2(\Omega)$. These subspaces are spanned by basis functions

$$\text{span}\{\psi_1, \dots, \psi_{d_p}\} = \mathcal{P}_h, \quad \text{span}\{\boldsymbol{\alpha}_1, \dots, \boldsymbol{\alpha}_{d_w}\} = \mathcal{W}_h, \quad \text{span}\{\boldsymbol{\beta}_1, \dots, \boldsymbol{\beta}_{d_u}\} = \mathcal{U}_h, \quad \text{and} \quad \text{span}\{\gamma_1, \dots, \gamma_{d_q}\} = \mathcal{Q}_h, \quad (8)$$

with d_p , d_w , d_u , and d_q , the number of degrees of freedom of the spaces \mathcal{P}_h , \mathcal{W}_h , \mathcal{U}_h , and \mathcal{Q}_h , respectively. The basis functions themselves are constructed by tensor product combinations of nodal and edge polynomials [12]. As usual, elements of these spaces can be represented as a linear combination of the basis functions, for example, for $p_h \in \mathcal{P}_h$, $\mathbf{w}_h \in \mathcal{W}_h$, $\mathbf{u}_h \in \mathcal{U}_h$, and $c_h \in \mathcal{Q}_h$ we have that

$$p_h = \sum_{i=1}^{d_p} \hat{p}_i \psi_i, \quad \mathbf{w}_h = \sum_{i=1}^{d_w} \hat{w}_i \boldsymbol{\alpha}_i, \quad \mathbf{u}_h = \sum_{i=1}^{d_u} \hat{u}_i \boldsymbol{\beta}_i, \quad \text{and} \quad c_h = \sum_{i=1}^{d_q} \hat{c}_i \gamma_i. \quad (9)$$

We now introduce an equivalent, but more compact, notation for the expansion of a function as a linear combination of the basis functions

$$p_h = \boldsymbol{\psi}_h \hat{\mathbf{p}}_h, \quad \mathbf{w}_h = \boldsymbol{\alpha}_h \hat{\mathbf{w}}_h, \quad \mathbf{u}_h = \boldsymbol{\beta}_h \hat{\mathbf{u}}_h, \quad \text{and} \quad c_h = \boldsymbol{\gamma}_h \hat{c}_h, \quad (10)$$

where $\hat{\mathbf{p}}_h := [p_1, \dots, p_{d_p}]^\top$, $\hat{\mathbf{w}}_h := [w_1, \dots, w_{d_w}]^\top$, $\hat{\mathbf{u}}_h := [u_1, \dots, u_{d_u}]^\top$, and $\hat{c}_h := [c_1, \dots, c_{d_q}]^\top$ are the column vectors containing the coefficients of the discrete representation of the associated functions, and $\boldsymbol{\psi}_h := [\psi_1, \dots, \psi_{d_p}]$, $\boldsymbol{\alpha}_h := [\boldsymbol{\alpha}_1, \dots, \boldsymbol{\alpha}_{d_w}]$, $\boldsymbol{\beta}_h := [\boldsymbol{\beta}_1, \dots, \boldsymbol{\beta}_{d_u}]$, and $\boldsymbol{\gamma}_h := [\gamma_1, \dots, \gamma_{d_q}]$ are the row vectors containing the basis functions.

Remark 1. Throughout this work we will extensively use the basis functions $\boldsymbol{\psi}_h$, $\boldsymbol{\alpha}_h$, $\boldsymbol{\beta}_h$, and $\boldsymbol{\gamma}_h$. For clarity in the notation, these symbols will be solely used to refer to the basis functions:

$$\begin{aligned} \boldsymbol{\psi}_h &:= [\psi_1, \dots, \psi_{d_p}] & \text{such that} & \quad \text{span}\{\psi_1, \dots, \psi_{d_p}\} = \mathcal{P}_h \\ \boldsymbol{\alpha}_h &:= [\boldsymbol{\alpha}_1, \dots, \boldsymbol{\alpha}_{d_w}] & \text{such that} & \quad \text{span}\{\boldsymbol{\alpha}_1, \dots, \boldsymbol{\alpha}_{d_w}\} = \mathcal{W}_h \\ \boldsymbol{\beta}_h &:= [\boldsymbol{\beta}_1, \dots, \boldsymbol{\beta}_{d_u}] & \text{such that} & \quad \text{span}\{\boldsymbol{\beta}_1, \dots, \boldsymbol{\beta}_{d_u}\} = \mathcal{U}_h \\ \boldsymbol{\gamma}_h &:= [\gamma_1, \dots, \gamma_{d_q}] & \text{such that} & \quad \text{span}\{\gamma_1, \dots, \gamma_{d_q}\} = \mathcal{Q}_h. \end{aligned} \quad (11)$$

These discrete function spaces satisfy a compatibility relation that is expressed as a discrete de Rham complex similar to the continuous one

$$\mathbb{R} \longrightarrow \mathcal{P}_h \xrightarrow{\nabla} \mathcal{W}_h \xrightarrow{\nabla \times} \mathcal{U}_h \xrightarrow{\nabla \cdot} \mathcal{Q}_h \longrightarrow 0. \quad (12)$$

The differential operators ∇ , $\nabla \times$, and $\nabla \cdot$ are efficiently represented at the discrete level by incidence matrices, $\mathbf{E}^{1,0}$, $\mathbf{E}^{2,1}$, $\mathbf{E}^{3,2}$, such that for $p_h \in \mathcal{P}_h$, $\mathbf{w}_h \in \mathcal{W}_h$, and $\mathbf{u}_h \in \mathcal{U}_h$ we have that

$$\nabla p_h = \boldsymbol{\alpha}_h \mathbf{E}^{1,0} \hat{\mathbf{p}}_h, \quad \nabla \times \mathbf{w}_h = \boldsymbol{\beta}_h \mathbf{E}^{2,1} \hat{\mathbf{w}}_h, \quad \text{and} \quad \nabla \cdot \mathbf{u}_h = \boldsymbol{\gamma}_h \mathbf{E}^{3,2} \hat{\mathbf{u}}_h. \quad (13)$$

In a similar way, we may apply the differential operators to the basis functions ψ_h , α_h , β_h , and γ_h yielding

$$\nabla\psi_h = \alpha_h \mathbf{E}^{1,0}, \quad \nabla \times \alpha_h = \beta_h \mathbf{E}^{2,1}, \quad \text{and} \quad \nabla \cdot \beta_h = \gamma_h \mathbf{E}^{3,2}. \quad (14)$$

These incidence matrices satisfy the identities

$$\mathbf{E}^{2,1} \mathbf{E}^{1,0} = \mathbf{0}^{2,0}, \quad \text{and} \quad \mathbf{E}^{3,2} \mathbf{E}^{2,1} = \mathbf{0}^{3,1}, \quad (15)$$

where $\mathbf{0}^{2,0}$ is the $d_{\mathcal{U}} \times d_{\mathcal{P}}$ zero matrix and $\mathbf{0}^{3,1}$ is the $d_{\mathcal{Q}} \times d_{\mathcal{W}}$ zero matrix. Note that these two identities are directly related to the well known vector calculus identities $\nabla \times \nabla = 0$ and $\nabla \cdot \nabla \times = 0$. For a more detailed discussion of the incidence matrices and their properties the reader is directed to [14].

Additionally, these compatible function spaces satisfy an integration-by-parts property, such that the reverse mappings $(\tilde{\nabla} \cdot, \tilde{\nabla} \times, \tilde{\nabla})$, satisfy

$$0 \leftarrow \mathcal{P}_h \xleftarrow{\tilde{\nabla} \cdot} \mathcal{W}_h \xleftarrow{\tilde{\nabla} \times} \mathcal{U}_h \xleftarrow{\tilde{\nabla}} \mathcal{Q}_h \leftarrow \mathbb{R}. \quad (16)$$

and are represented by weak form adjoint relations. Assuming periodic or homogeneous boundary conditions we have that for $w_h \in \mathcal{W}_h$, $u_h \in \mathcal{U}_h$, and $c_h \in \mathcal{Q}_h$

$$\begin{aligned} \langle \beta_h, \tilde{\nabla} c_h \rangle &= -\langle \nabla \cdot \beta_h, c_h \rangle, \\ \langle \alpha_h, \tilde{\nabla} \times u_h \rangle &= \langle \nabla \times \alpha_h, u_h \rangle, \\ \langle \psi_h, \tilde{\nabla} \cdot w_h \rangle &= -\langle \nabla \psi_h, w_h \rangle. \end{aligned} \quad (17)$$

Remark 2. In (17) we have used an implicit matrix notation. As an example, consider the expression $\langle \beta_h, \beta_h \rangle$. This expression corresponds to

$$\langle \beta_h, \beta_h \rangle := \int_{\Omega} \beta_h^{\top} \beta_h \, d\Omega, \quad (18)$$

which is a matrix of dimensions $d_{\mathcal{U}} \times d_{\mathcal{U}}$ with element (i, j) , $\langle \beta_h, \beta_h \rangle_{i,j}$, given by

$$\langle \beta_h, \beta_h \rangle_{i,j} = \langle \beta_i, \beta_j \rangle.$$

As a more complex example, consider the expression $\langle \nabla \psi_h, w_h \rangle$, with $w_h \in \mathcal{W}_h$. In a similar way, this expression corresponds to

$$\langle \nabla \psi_h, w_h \rangle = \int_{\Omega} \nabla \psi_h^{\top} w_h \, d\Omega,$$

which is a column vector of $d_{\mathcal{W}}$ elements with element j , $\langle \nabla \psi_h, w_h \rangle_j$, given by

$$\langle \nabla \psi_h, w_h \rangle_j \stackrel{(18)}{=} \left(\int_{\Omega} \nabla \psi_h^{\top} w_h \right)_j \stackrel{(14)}{=} \left(\int_{\Omega} (\mathbf{E}^{1,0})^{\top} \alpha_h^{\top} w_h \right)_j = \left((\mathbf{E}^{1,0})^{\top} \langle \alpha_h, w_h \rangle \right)_j = \sum_{k=1}^{d_{\mathcal{W}}} \mathbf{E}_{k,j}^{1,0} \langle \alpha_k, w_h \rangle.$$

This leads to the following discrete representations of the dual operators applied to $w_h \in \mathcal{P}_h$, $u_h \in \mathcal{U}_h$, and $c_h \in \mathcal{Q}_h$

$$\begin{aligned} \tilde{\nabla} c_h &= -\beta_h \langle \beta_h, \beta_h \rangle^{-1} (\mathbf{E}^{3,2})^{\top} \langle \gamma_h, \gamma_h \rangle \hat{c}_h, \\ \tilde{\nabla} \times u_h &= \alpha_h \langle \alpha_h, \alpha_h \rangle^{-1} (\mathbf{E}^{2,1})^{\top} \langle \beta_h, \beta_h \rangle \hat{u}_h, \\ \tilde{\nabla} \cdot w_h &= \psi_h \langle \psi_h, \psi_h \rangle^{-1} (\mathbf{E}^{1,0})^{\top} \langle \alpha_h, \alpha_h \rangle \hat{w}_h. \end{aligned} \quad (19)$$

The discrete form of the variational 3D compressible Euler equations (4) may then be expressed as: Given $u_h|_{t=0} \in \mathcal{U}$, $\rho|_{t=0}$, $\Theta|_{t=0} \in \mathcal{Q}$, find $u_h \in \mathcal{U}$, ρ , $\Theta \in \mathcal{Q}$ such that

$$\left\langle \beta_h, \frac{\partial u_h}{\partial t} \right\rangle = -\langle \beta_h, q_h \times U_h \rangle + \langle \nabla \cdot \beta_h, \Phi_h \rangle + \langle \nabla \cdot \mathbb{P}^{\text{div}} [\theta_h \beta_h], \Pi_h \rangle, \quad (20a)$$

$$\left\langle \gamma_h, \frac{\partial \rho_h}{\partial t} \right\rangle = -\langle \gamma_h, \nabla \cdot U_h \rangle, \quad (20b)$$

$$\left\langle \gamma_h, \frac{\partial \Theta_h}{\partial t} \right\rangle = -\langle \gamma_h, \nabla \cdot \mathbb{P}^{\text{div}} [\theta_h U_h] \rangle, \quad (20c)$$

and $\mathbf{U}_h \in \mathcal{U}$, $\Phi_h, \Pi_h \in \mathcal{Q}$ such that

$$\langle \boldsymbol{\beta}_h, \frac{\delta H_h}{\delta \mathbf{u}_h} \rangle = \langle \boldsymbol{\beta}_h, \mathbf{U}_h \rangle = \langle \boldsymbol{\beta}_h, \rho_h \mathbf{u}_h \rangle, \quad (21a)$$

$$\langle \gamma_h, \frac{\delta H_h}{\delta \rho_h} \rangle = \langle \gamma_h, \Phi_h \rangle = \langle \gamma_h, \frac{1}{2} \mathbf{u}_h \cdot \mathbf{u}_h + gz \rangle, \quad (21b)$$

$$\langle \gamma_h, \frac{\delta H_h}{\delta \Theta_h} \rangle = \langle \gamma_h, \Pi_h \rangle = \langle \gamma_h, c_p \left(\frac{R \Theta_h}{p_0} \right)^{\frac{R}{c_p}} \rangle. \quad (21c)$$

This problem can be stated in a fully discrete form as:

$$\begin{aligned} \begin{bmatrix} \langle \boldsymbol{\beta}_h, \boldsymbol{\beta}_h \rangle \hat{\mathbf{u}}_h^{n+1} \\ \langle \gamma_h, \gamma_h \rangle \hat{\rho}_h^{n+1} \\ \langle \gamma_h, \gamma_h \rangle \hat{\Theta}_h^{n+1} \end{bmatrix} &= \begin{bmatrix} \langle \boldsymbol{\beta}_h, \boldsymbol{\beta}_h \rangle \hat{\mathbf{u}}_h^n \\ \langle \gamma_h, \gamma_h \rangle \hat{\rho}_h^n \\ \langle \gamma_h, \gamma_h \rangle \hat{\Theta}_h^n \end{bmatrix} - \\ \Delta t \begin{bmatrix} \langle \boldsymbol{\beta}_h, \mathbf{q}_h^{n+\frac{1}{2}} \times \boldsymbol{\beta}_h \rangle & -(\mathbf{E}^{3,2})^\top \langle \gamma_h, \gamma_h \rangle & -\langle \boldsymbol{\beta}_h, \theta_h^{n+\frac{1}{2}} \boldsymbol{\beta}_h \rangle \langle \boldsymbol{\beta}_h, \boldsymbol{\beta}_h \rangle^{-1} (\mathbf{E}^{3,2}) \langle \gamma_h, \gamma_h \rangle \\ \langle \gamma_h, \gamma_h \rangle \mathbf{E}^{3,2} & 0 & 0 \\ \langle \gamma_h, \gamma_h \rangle \mathbf{E}^{3,2} \langle \boldsymbol{\beta}_h, \boldsymbol{\beta}_h \rangle^{-1} \langle \boldsymbol{\beta}_h, \theta_h^{n+\frac{1}{2}} \boldsymbol{\beta}_h \rangle & 0 & 0 \end{bmatrix} \begin{bmatrix} \bar{\mathbf{U}}_h \\ \bar{\Phi}_h \\ \bar{\Pi}_h \end{bmatrix}. \end{aligned} \quad (22)$$

where $\bar{\mathbf{U}}_h$, $\bar{\Phi}_h$, and $\bar{\Pi}_h$ are the exact time integrals of the discrete piecewise linear approximation of the variational derivatives between time levels n and $n+1$ to be described in the proceeding section, and $\theta_h^{n+\frac{1}{2}} = (\theta_h^n + \theta_h^{n+1})/2$, $\mathbf{q}_h^{n+\frac{1}{2}} = (\mathbf{q}_h^n + \mathbf{q}_h^{n+1})/2$ are the time centered potential temperature and potential vorticity.

3. HEVI splitting

The above system (22) may be dimensionally split into an implicit solve for the vertical dynamics (incorporating the horizontal divergence terms) and explicit momentum advection by defining the horizontal and vertical velocity components respectively as $\mathbf{v}_h \in \mathcal{U}_h^\parallel$, $\mathbf{w}_h \in \mathcal{U}_h^\perp$, such that $\mathbf{u}_h = \mathbf{v}_h + \mathbf{w}_h \in \mathcal{U}_h$. Similarly, the discrete strong form divergence operator, as given by the incidence matrix $\mathbf{E}^{3,2}$, may itself be decomposed into its horizontal, $\mathbf{E}_\parallel^{3,2}$ and vertical $\mathbf{E}_\perp^{3,2}$ components, such that

$$\nabla \cdot \mathbf{u}_h \stackrel{(13)}{=} \gamma_h \mathbf{E}^{3,2} \hat{\mathbf{u}}_h =: \gamma_h (\mathbf{E}_\parallel^{3,2} \hat{\mathbf{v}}_h + \mathbf{E}_\perp^{3,2} \hat{\mathbf{w}}_h). \quad (23)$$

The second order HEVI splitting is then given as:

Step 1: Explicit horizontal momentum solve

$$\langle \boldsymbol{\beta}_h^\parallel, \boldsymbol{\beta}_h^\parallel \rangle \hat{\mathbf{v}}_h' = \langle \boldsymbol{\beta}_h^\parallel, \boldsymbol{\beta}_h^\parallel \rangle \hat{\mathbf{v}}_h^{n-1} - 2\Delta t \langle \boldsymbol{\beta}_h^\parallel, \mathbf{q}_h^n \times \boldsymbol{\beta}_h^\parallel \rangle \hat{\mathbf{v}}_h^n + 2\Delta t (\mathbf{E}_\parallel^{3,2})^\top \langle \gamma_h, \gamma_h \rangle \hat{\Phi}_h^n + 2\Delta t (\mathbf{E}_\parallel^{3,2})^\top \langle \gamma_h, \theta_h^n \gamma_h \rangle \hat{\Pi}_h^n \quad (24)$$

Step 2: Implicit vertical solve (including horizontal divergence)

$$\begin{aligned} \begin{bmatrix} \langle \boldsymbol{\beta}_h^\perp, \boldsymbol{\beta}_h^\perp \rangle \hat{\mathbf{w}}_h^{n+1} \\ \langle \gamma_h, \gamma_h \rangle \hat{\rho}_h^{n+1} \\ \langle \gamma_h, \gamma_h \rangle \hat{\Theta}_h^{n+1} \end{bmatrix} &= \begin{bmatrix} \langle \boldsymbol{\beta}_h^\perp, \boldsymbol{\beta}_h^\perp \rangle \hat{\mathbf{w}}_h^n \\ \langle \gamma_h, \gamma_h \rangle \hat{\rho}_h^n \\ \langle \gamma_h, \gamma_h \rangle \hat{\Theta}_h^n \end{bmatrix} - \\ \Delta t \begin{bmatrix} \langle \boldsymbol{\beta}_h^\perp, \mathbf{q}_h^{n+1/2} \times \boldsymbol{\beta}_h^\perp \rangle & -(\mathbf{E}_\perp^{3,2})^\top \langle \gamma_h, \gamma_h \rangle & -\langle \boldsymbol{\beta}_h^\perp, \theta_h^{n+1/2} \boldsymbol{\beta}_h^\perp \rangle \langle \boldsymbol{\beta}_h^\perp, \boldsymbol{\beta}_h^\perp \rangle^{-1} (\mathbf{E}_\perp^{3,2})^\top \langle \gamma_h, \gamma_h \rangle \\ \langle \gamma_h, \gamma_h \rangle \mathbf{E}_\perp^{3,2} & 0 & 0 \\ \langle \gamma_h, \gamma_h \rangle \mathbf{E}_\perp^{3,2} \langle \boldsymbol{\beta}_h^\perp, \boldsymbol{\beta}_h^\perp \rangle^{-1} \langle \boldsymbol{\beta}_h^\perp, \theta_h^{n+1/2} \boldsymbol{\beta}_h^\perp \rangle & 0 & 0 \end{bmatrix} \begin{bmatrix} \bar{\mathbf{W}}_h \\ \bar{\Phi}_h \\ \bar{\Pi}_h \end{bmatrix} - \\ \Delta t \begin{bmatrix} 0 \\ \langle \gamma_h, \gamma_h \rangle \mathbf{E}_\parallel^{3,2} \bar{\mathbf{V}}_h \\ \langle \gamma_h, \gamma_h \rangle \mathbf{E}_\parallel^{3,2} \langle \boldsymbol{\beta}_h^\parallel, \boldsymbol{\beta}_h^\parallel \rangle^{-1} \langle \boldsymbol{\beta}_h^\parallel, \theta_h^{n+1/2} \boldsymbol{\beta}_h^\parallel \rangle \bar{\mathbf{V}}_h \end{bmatrix} \end{aligned} \quad (25)$$

Step 3: Explicit horizontal momentum solve

$$\langle \boldsymbol{\beta}_h^{\parallel}, \boldsymbol{\beta}_h^{\parallel} \rangle \hat{v}_h^{n+1} = \langle \boldsymbol{\beta}_h^{\parallel}, \boldsymbol{\beta}_h^{\parallel} \rangle \hat{v}_h^n - \Delta t \langle \boldsymbol{\beta}_h^{\parallel}, \mathbf{q}_h^{n+1/2} \times \boldsymbol{\beta}_h^{\parallel} \rangle \bar{V}_h + \Delta t (\mathbf{E}_{\parallel}^{3,2})^{\top} \langle \gamma_h, \gamma_h \rangle \bar{\Phi}_h + \Delta t (\mathbf{E}_{\parallel}^{3,2})^{\top} \langle \gamma_h, \theta_h^{n+1/2} \gamma_h \rangle \bar{\Pi}_h \quad (26)$$

Left multiplication of (25) by $[\bar{W}_h^{\top} \quad \bar{\Phi}_h^{\top} \quad \bar{\Pi}_h^{\top}]$ and (26) by \bar{V}_h^{\top} leads to the cancellation of all forcing terms in both equations, resulting in the expression

$$\bar{V}_h \langle \boldsymbol{\beta}_h^{\parallel}, \boldsymbol{\beta}_h^{\parallel} \rangle (\hat{v}_h^{n+1} - \hat{v}_h^n) + \bar{W}_h \langle \boldsymbol{\beta}_h^{\parallel}, \boldsymbol{\beta}_h^{\parallel} \rangle (\hat{w}_h^{n+1} - \hat{w}_h^n) + \bar{\Phi}_h \langle \gamma_h, \gamma_h \rangle (\hat{\rho}_h^{n+1} - \hat{\rho}_h^n) + \bar{\Pi}_h \langle \gamma_h, \gamma_h \rangle (\hat{\Theta}_h^{n+1} - \hat{\Theta}_h^n) = 0 \quad (27)$$

Note that since \mathbf{v}_h^n and \mathbf{v}_h^{n+1} differ energy is not strictly conserved in the temporal discretisation of the horizontal momentum equation, since (27) is not strictly a discrete analogue of the continuous expression

$$\left(\frac{\delta H}{\delta \mathbf{a}} \right)^{\top} \cdot \frac{\partial \mathbf{a}}{\partial t} \neq 0. \quad (28)$$

The above formulation is similar to the "u-forward, pressure-backward" formulation [6], by which the horizontal divergence term is treated implicitly (using the most recent horizontal velocity update), and the horizontal pressure gradient term is treated explicitly. However in the present case the horizontal pressure gradient term at the final step is evaluated at the same time level as the (implicit) horizontal divergence term.

In order to ensure second order accuracy in time, the variational derivatives are given as:

$$\langle \boldsymbol{\beta}_h^{\parallel}, \boldsymbol{\beta}_h^{\parallel} \rangle \bar{V}_h = \frac{1}{3} \langle \boldsymbol{\beta}_h^{\parallel}, \rho_h^n \boldsymbol{\beta}_h^{\parallel} \rangle \hat{v}_h^n + \frac{1}{6} \langle \boldsymbol{\beta}_h^{\parallel}, \rho_h^{n+1} \boldsymbol{\beta}_h^{\parallel} \rangle \hat{v}_h^n + \frac{1}{6} \langle \boldsymbol{\beta}_h^{\parallel}, \rho_h^n \boldsymbol{\beta}_h^{\parallel} \rangle \hat{v}_h' + \frac{1}{3} \langle \boldsymbol{\beta}_h^{\parallel}, \rho_h^{n+1} \boldsymbol{\beta}_h^{\parallel} \rangle \hat{v}_h' \quad (29a)$$

$$\langle \boldsymbol{\beta}_h^{\perp}, \boldsymbol{\beta}_h^{\perp} \rangle \bar{W}_h = \frac{1}{3} \langle \boldsymbol{\beta}_h^{\perp}, \rho_h^n \boldsymbol{\beta}_h^{\perp} \rangle \hat{w}_h^n + \frac{1}{6} \langle \boldsymbol{\beta}_h^{\perp}, \rho_h^{n+1} \boldsymbol{\beta}_h^{\perp} \rangle \hat{w}_h^n + \frac{1}{6} \langle \boldsymbol{\beta}_h^{\perp}, \rho_h^n \boldsymbol{\beta}_h^{\perp} \rangle \hat{w}_h^{n+1} + \frac{1}{3} \langle \boldsymbol{\beta}_h^{\perp}, \rho_h^{n+1} \boldsymbol{\beta}_h^{\perp} \rangle \hat{w}_h^{n+1} \quad (29b)$$

$$\begin{aligned} \langle \gamma_h, \gamma_h \rangle \bar{\Phi}_h &= \frac{1}{6} \langle \gamma_h, \mathbf{v}_h^n \cdot \boldsymbol{\beta}_h^{\parallel} \rangle \hat{v}_h^n + \frac{1}{6} \langle \gamma_h, \mathbf{v}_h' \cdot \boldsymbol{\beta}_h^{\parallel} \rangle \hat{v}_h^n + \frac{1}{6} \langle \gamma_h, \mathbf{v}_h' \cdot \boldsymbol{\beta}_h^{\parallel} \rangle \hat{v}_h' + \\ &\quad \frac{1}{6} \langle \gamma_h, w_h^n \boldsymbol{\beta}_h^{\perp} \rangle \hat{w}_h^n + \frac{1}{6} \langle \gamma_h, w_h^{n+1} \boldsymbol{\beta}_h^{\perp} \rangle \hat{w}_h^n + \frac{1}{6} \langle \gamma_h, w_h^{n+1} \boldsymbol{\beta}_h^{\perp} \rangle \hat{w}_h^{n+1} + g \langle \gamma_h, \gamma_h \rangle \hat{z}_h \end{aligned} \quad (29c)$$

$$\langle \gamma_h, \gamma_h \rangle \bar{\Pi}_h = \frac{1}{2} \langle \gamma_h, \gamma_h \rangle \hat{\Pi}_h^n + \frac{1}{2} \langle \gamma_h, \gamma_h \rangle \hat{\Pi}_h^{n+1} \quad (29d)$$

Note that while a second order "leap-frog" method has been used to determine the provisional velocity, \hat{v}_h' in (24), a first order, forward Euler step is probably also acceptable, since in either case the resulting mass flux (29a) will be second order in time.

3.1. Stability analysis

In order to study the stability of the HEVI splitting scheme described above this is applied to the two dimensional linearised compressible Boussinesq equations [17], which are given as:

$$\frac{\partial u}{\partial t} + \frac{\partial p}{\partial x} = 0 \quad (30a)$$

$$\frac{\partial w}{\partial t} + \frac{\partial p}{\partial z} - b = 0 \quad (30b)$$

$$\frac{\partial p}{\partial t} + c^2 \left(\frac{\partial u}{\partial x} + \frac{\partial w}{\partial z} \right) = 0 \quad (30c)$$

$$\frac{\partial b}{\partial t} + N^2 w = 0 \quad (30d)$$

where u and w are the horizontal and vertical velocities, p is the pressure, b is the buoyancy, c is the speed of sound and N is the Brunt-Väisälä frequency. Using the splitting scheme detailed above (but with a first order forward Euler

step for the initial provisional velocity, u') and assuming periodic solutions of the form $(u, w, p, b)(t)e^{ikx+ilz}$ these may be time-stepped as:

$$u' = u^n - \Delta tik p^n \quad (31a)$$

$$w^{n+1} + \frac{\Delta til}{2} p^{n+1} - \frac{\Delta t}{2} b^{n+1} = w^n - \frac{\Delta til}{2} p^n + \frac{\Delta t}{2} b^n \quad (31b)$$

$$p^{n+1} + \frac{\Delta tilc^2}{2} w^{n+1} = p^n - \frac{\Delta tilc^2}{2} w^n - \frac{\Delta tikc^2}{2} u^n - \frac{\Delta tikc^2}{2} u' \quad (31c)$$

$$b^{n+1} + \frac{\Delta tN^2}{2} w^{n+1} = b^n - \frac{\Delta tN^2}{2} w^n \quad (31d)$$

$$u^{n+1} + \frac{\Delta tik}{2} p^{n+1} = u^n - \frac{\Delta tik}{2} p^n \quad (31e)$$

Substituting the expression for u' into that for p^{n+1} and expressing in matrix form gives

$$\begin{bmatrix} 1 & 0 & \frac{\Delta tik}{2} & 0 \\ 0 & 1 & \frac{\Delta til}{2} & -\frac{\Delta t}{2} \\ 0 & \frac{\Delta tilc^2}{2} & 1 & 0 \\ 0 & \frac{\Delta tN^2}{2} & 0 & 1 \end{bmatrix} \begin{bmatrix} u^{n+1} \\ w^{n+1} \\ p^{n+1} \\ b^{n+1} \end{bmatrix} = \begin{bmatrix} 1 & 0 & -\frac{\Delta tik}{2} & 0 \\ 0 & 1 & -\frac{\Delta til}{2} & \frac{\Delta t}{2} \\ -\Delta tikc^2 & -\frac{\Delta tilc^2}{2} & 1 - \frac{\Delta t^2 k^2 c^2}{2} & 0 \\ 0 & -\frac{\Delta tN^2}{2} & 0 & 1 \end{bmatrix} \begin{bmatrix} u^n \\ w^n \\ p^n \\ b^n \end{bmatrix} \quad (32)$$

In order to analyse the stability of the splitting scheme we inspect the eigenvalues of the operator

$$\mathbf{A} = \begin{bmatrix} 1 & 0 & \frac{\Delta tik}{2} & 0 \\ 0 & 1 & \frac{\Delta til}{2} & -\frac{\Delta t}{2} \\ 0 & \frac{\Delta tilc^2}{2} & 1 & 0 \\ 0 & \frac{\Delta tN^2}{2} & 0 & 1 \end{bmatrix}^{-1} \begin{bmatrix} 1 & 0 & -\frac{\Delta tik}{2} & 0 \\ 0 & 1 & -\frac{\Delta til}{2} & \frac{\Delta t}{2} \\ -\Delta tikc^2 & -\frac{\Delta tilc^2}{2} & 1 - \frac{\Delta t^2 k^2 c^2}{2} & 0 \\ 0 & -\frac{\Delta tN^2}{2} & 0 & 1 \end{bmatrix} \quad (33)$$

For a given eigenvalue, λ_i , this will be unstable if $\lambda_i \lambda_i^* > 1$. The four eigenvalues correspond to two acoustic modes, which differ in the sign of their imaginary component only, and two gravity (buoyancy) modes which similarly differ only in the sign of the imaginary term.

The results for the new HEVI scheme are compared to the standard second order trapezoidal HEVI scheme, for which the vertical terms are all treated implicitly, and the horizontal terms explicitly. This scheme may be written as:

$$\begin{bmatrix} 1 & 0 & 0 & 0 \\ 0 & 1 & \frac{\Delta til}{2} & -\frac{\Delta t}{2} \\ 0 & \frac{\Delta tilc^2}{2} & 1 & 0 \\ 0 & \frac{\Delta tN^2}{2} & 0 & 1 \end{bmatrix} \begin{bmatrix} u' \\ w' \\ p' \\ b' \end{bmatrix} = \begin{bmatrix} 1 & 0 & -\Delta tik & 0 \\ 0 & 1 & -\frac{\Delta til}{2} & \frac{\Delta t}{2} \\ -\Delta tikc^2 & -\frac{\Delta tilc^2}{2} & 1 & 0 \\ 0 & \frac{\Delta tN^2}{2} & 0 & 1 \end{bmatrix} \begin{bmatrix} u^n \\ w^n \\ p^n \\ b^n \end{bmatrix} \quad (34)$$

$$\begin{bmatrix} u^{n+1} \\ w^{n+1} \\ p^{n+1} \\ b^{n+1} \end{bmatrix} = \begin{bmatrix} 1 & 0 & -\frac{\Delta tik}{2} & 0 \\ 0 & 1 & -\frac{\Delta til}{2} & \frac{\Delta t}{2} \\ -\frac{\Delta tikc^2}{2} & -\frac{\Delta tilc^2}{2} & 1 & 0 \\ 0 & -\frac{\Delta tN^2}{2} & 0 & 1 \end{bmatrix} \begin{bmatrix} u^n \\ w^n \\ p^n \\ b^n \end{bmatrix} + \begin{bmatrix} 0 & 0 & -\frac{\Delta tik}{2} & 0 \\ 0 & 0 & -\frac{\Delta til}{2} & \frac{\Delta t}{2} \\ -\frac{\Delta tikc^2}{2} & -\frac{\Delta tilc^2}{2} & 0 & 0 \\ 0 & -\frac{\Delta tN^2}{2} & 0 & 0 \end{bmatrix} \begin{bmatrix} u' \\ w' \\ p' \\ b' \end{bmatrix} \quad (35)$$

Combining the above expressions gives a linear operator by which the solution at time level $n + 1$ may be determined from the solution at time level n , from which the corresponding eigenvalues may be derived.

For completeness we also compare against the Crank-Nicholson scheme, which is semi-implicit in both horizontal and vertical dimensions, and neutrally stable for all vertical and horizontal wave numbers for both buoyancy and acoustic modes. The amplification factors for the Crank-Nicolson scheme are given as:

$$\mathbf{A} = \begin{bmatrix} 1 & 0 & \frac{\Delta tik}{2} & 0 \\ 0 & 1 & \frac{\Delta til}{2} & -\frac{\Delta t}{2} \\ \frac{\Delta tilc^2}{2} & \frac{\Delta tilc^2}{2} & 1 & 0 \\ 0 & \frac{\Delta tN^2}{2} & 0 & 1 \end{bmatrix}^{-1} \begin{bmatrix} 1 & 0 & -\frac{\Delta tik}{2} & 0 \\ 0 & 1 & -\frac{\Delta til}{2} & \frac{\Delta t}{2} \\ -\frac{\Delta tikc^2}{2} & -\frac{\Delta tilc^2}{2} & 1 & 0 \\ 0 & -\frac{\Delta tN^2}{2} & 0 & 1 \end{bmatrix} \quad (36)$$

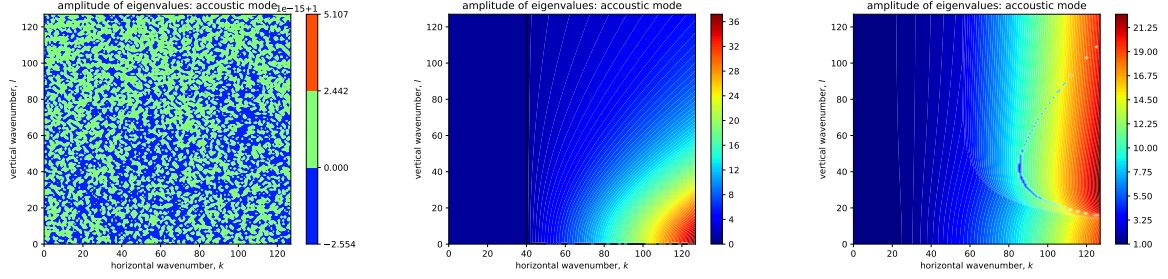


Figure 1: Amplification factor for the acoustic waves using the Crank-Nicholson (left), new (center) and trapezoidal HEVI (right) splitting. The black line on the center plot indicates an amplification factor of $1.0 + 10^{-7}$, indicating the onset of unstable modes.

The amplification factors for the acoustic and gravity modes for the three different time splitting schemes are given in figs. 1 and 2 respectively for a periodic domain of size 1000.0m in both dimensions, with $c = 340.0\text{ms}^{-1}$, $N = 0.01\text{s}^{-1}$. While the Crank-Nicholson scheme is neutrally stable, $|\lambda| = 1$ for both modes, and the trapezoidal HEVI scheme is unstable, $|\lambda| > 1$ for both modes, the energetically balanced splitting scheme is neutrally stable for all acoustic modes below some horizontal wave number, and unconditionally stable for all gravity modes. This represents a qualitative improvement on the standard second order HEVI splitting.

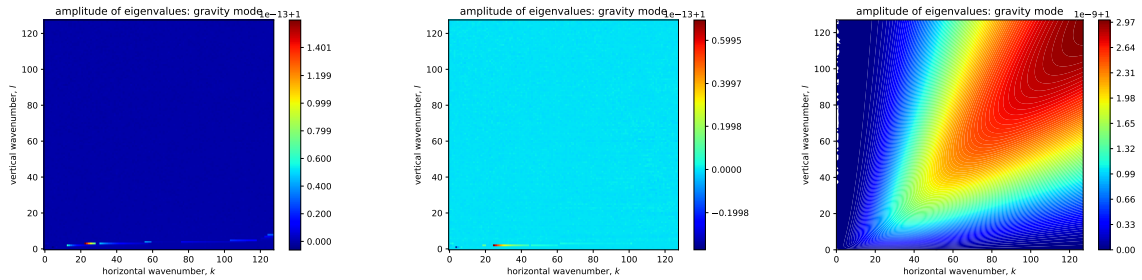


Figure 2: Amplification factor for the gravity waves using the Crank-Nicholson (left), new (center) and trapezoidal HEVI (right) splitting

4. Potential temperature upwinding

This section describes the suppression of spurious oscillations in potential temperature via upwinding of the potential temperature diagnostic equation in an energetically consistent manner. Since the potential vorticity and potential temperature are represented within the skew-symmetric operator for the discrete variational form of the compressible Euler equations(22), these quantities may be upwinded so as to suppress oscillations without breaking energy conservation (so long as skew-symmetry is preserved). This strategy has been used previously to suppress oscillations for the shallow water equations by upwinding potential vorticity so as to dissipate potential enstrophy [18–20], and for the compressible Euler equations by upwinding potential temperature so as to generate entropy [21]. In the present context the upwinding of potential temperature is applied not to the material form advection equation, but rather to the diagnostic equation by which the potential temperature is derived from the prognostic variables of density (1b) and density-weighted potential temperature (1c).

While this is typically achieved for variational methods by augmenting the test space with a linear correction which allows for dissipation in the direction of the flow [22], in the present case this is achieved by integrating the test functions backwards along velocity characteristics [20]. Here the upwinding is applied in the vertical direction only. Since the discrete potential temperature is represented as $\theta_h \in \mathcal{U}_h^\perp$ [8], for which the vertical component of the

tensor product basis is represented by piecewise linear polynomials, for this case the upwinded bases are effectively equivalent to the SUPG method [21, 22], with the distinction that this upwinding is applied to the diagnostic equation, and not the material form of the advection equation.

The upwinded trial functions, $\beta_h^{\perp,u} \in \mathcal{U}_h^\perp$ are computed by evaluating the quadrature points at vertically *downwind* locations, ζ^d , which are computed to first order as [20]:

$$\zeta^d = \zeta + 0.5\Delta t \sum_i \hat{w}_i \beta_i^\perp(\xi, \eta, \zeta), \quad (37)$$

where ξ , η and ζ are the local element coordinates. Note that in the above expression the velocity is interpolated to its local element value, and not its global physical value. Note also that the choice to integrate the vertical quadrature points downwind for a time of $0.5\Delta t$ is arbitrary, and may be tuned to optimise the balance between reduced oscillation and less diffusive solutions. The upwinded trial functions are then evaluated as $\beta_h^{\perp,u} = \beta_h^\perp(\xi, \eta, \zeta^d)$. The upwinded potential temperature is then diagnosed as:

$$\langle \beta_h^{\perp,u}, \rho_h \beta_h^\perp \rangle_{\hat{\theta}_h} = \langle \beta_h^{\perp,u}, \gamma_h \rangle_{\hat{\Theta}_h}. \quad (38)$$

Note that in the above expression only the test functions for the potential temperature diagnostic equation are evaluated at upstream locations, while the trial functions remain static. Moreover since continuity is enforced only in the vertical direction for the trial space of the potential temperature, \mathcal{U}_h^\perp , it is only in this direction that upwinding has any material effect.

While the variational form of the compressible Euler equations (4) conserve entropy, $s = c_p \log(\theta) + s_0$ (see Appendix), this is not true in the discrete form, since transcendental functions such as logarithms cannot be integrated exactly in the discrete form. As such, while the upwinding of the test functions as described above will generate additional entropy, there are already additional entropy sources at the discrete level.

5. Results

5.1. Baroclinic instability

In order to verify the energetically balanced HEVI scheme, this is applied to the solution of a standard test case for baroclinic instability on the sphere [23]. This test involves a small perturbation to an otherwise hydrostatically and geostrophically balanced atmosphere, which over several days generates a baroclinic wave. Figures 3, 4 and 5 show the surface level Exner pressure, as well as the vertical vorticity component and potential temperature at a height of $z = 1.57\text{km}$ at days 8 and 10 respectively. These compare well against previously published results [9, 23]. The signature of the baroclinic instability is also observed in the perturbation to the steady hydrostatic pressure profile, for which a vertical cross section at 50°N is shown at days 8 and 10 in fig 6.

5.1.1. Comparison to TRAP(2,3,2)

The energetically balanced IMEX scheme is compared to the horizontally third order, vertically second order trapezoidal scheme, TRAP(2,3,2) [6, 7]. In most respects the energetics of the two schemes are similar, despite the fact that the TRAP(2,3,2) scheme is not energetically balanced, but is higher order in the horizontal (also a time step of $\Delta t = 60\text{s}$ is used for the energetically balanced scheme, while the TRAP(2,3,2) simulation was run with a time step of $\Delta t = 120\text{s}$).

The one respect in which the two schemes differ markedly is the potential to kinetic power exchanges, for which the energetically balanced scheme exhibits a higher frequency oscillation not present in the TRAP(2,3,2) scheme, as shown in fig. 7. Fourier analysis of these power exchanges, taken between days 6 and 10, shows that while the amplitudes of the low-frequency modes ($k < 10$) match each other closely, both solutions exhibit a secondary peak, which for the TRAP(2,3,2) scheme occurs at $k = 33$ (2.91 hours), while for the energetically balanced scheme this peak occurs at $k = 131$ (0.73 hours). Curiously, the secondary peak for the energetically balanced scheme is almost exactly four times the frequency observed for the TRAP(2,3,2) scheme. Since the secondary peak for the TRAP(2,3,2) scheme is closer in frequency to the low frequency modes, which exhibit very similar behaviour for both schemes, there is a danger that this secondary peak will alias onto these low frequency modes than there is for the energetically balanced scheme.

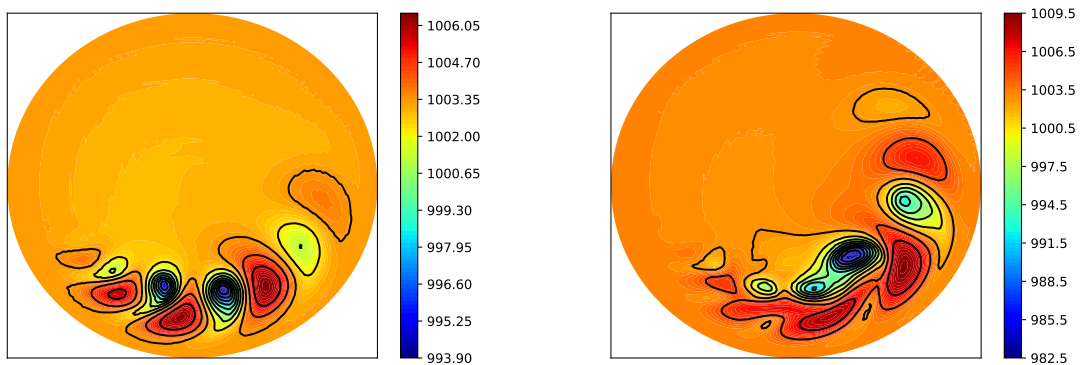


Figure 3: Bottom level Exner pressure, days 8 and 10.

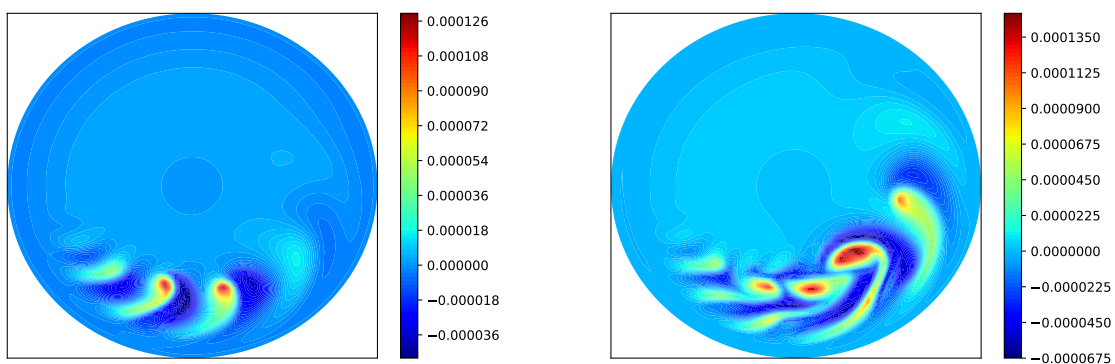


Figure 4: Vertical vorticity component at $z = 1.57\text{km}$, days 8 and 10.

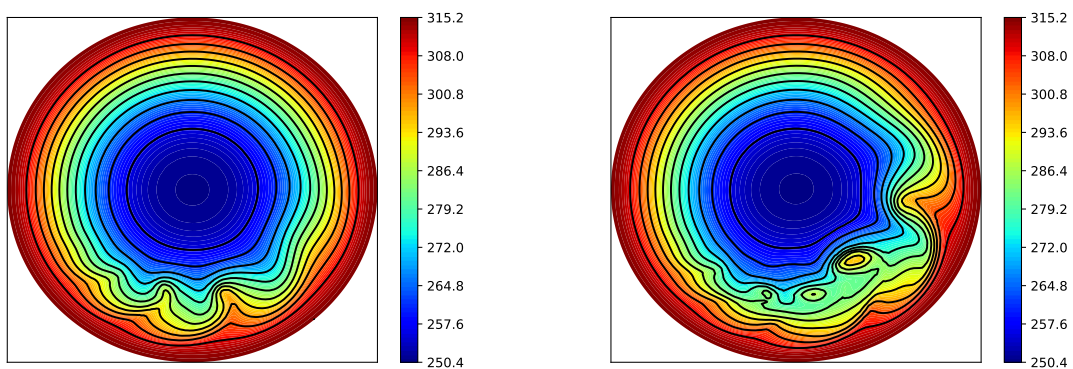


Figure 5: Potential temperature at $z = 1.57\text{km}$, days 8 and 10.

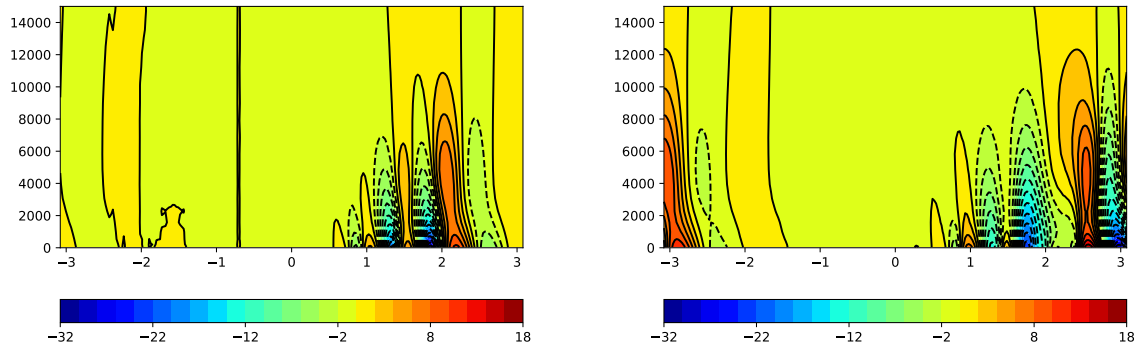


Figure 6: Zonal-vertical pressure slice at $50^\circ N$, days 8 and 10.

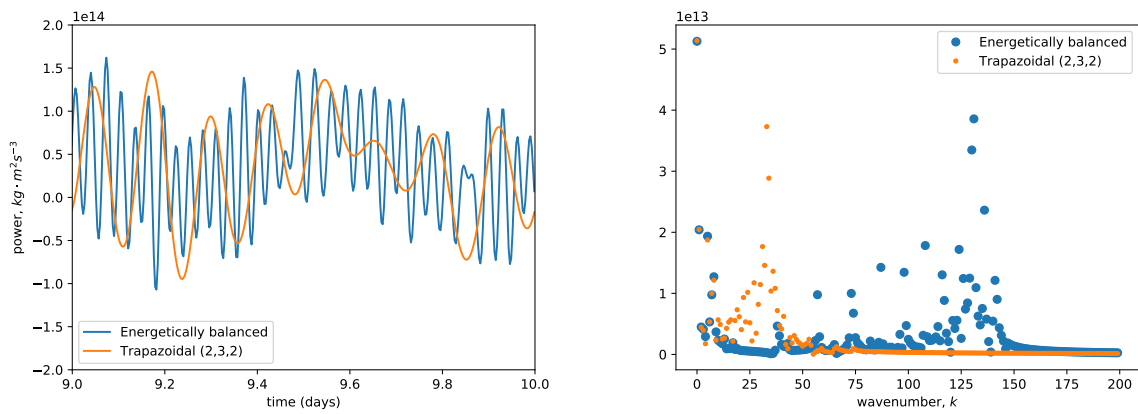


Figure 7: Comparison of potential to kinetic power exchanges for the energetically balanced and TRAP(2,3,2) IMEX schemes; left: real space from day 9 to 10, right: amplitude of the Fourier modes from days 6 to 10.

5.2. 3D Rising bubble

In order to verify the scheme for non-hydrostatic dynamics this is applied to a standard test case for a 3D rising bubble, which is initialised as a small perturbation in potential temperature against a constant background value, with the Exner pressure specified so as to satisfy hydrostatic balance [2, 24, 25]. The domain is configured as a horizontally periodic box of size $1000\text{m} \times 1000\text{m} \times 1500\text{m}$ with a flat bottom and top with homogeneous boundary conditions, which is discretised using 24×24 elements of degree $p = 3$ in the horizontal and 150 vertical levels, with a time step of $\Delta t = 0.01\text{s}$. The model is stabilised by the application of a biharmonic viscosity term to the horizontal momentum equation [11] with a coefficient of $624.78\text{m}^4\text{s}^{-1}$. No dissipation of any kind is applied in the vertical, or to the potential temperature advection equation.

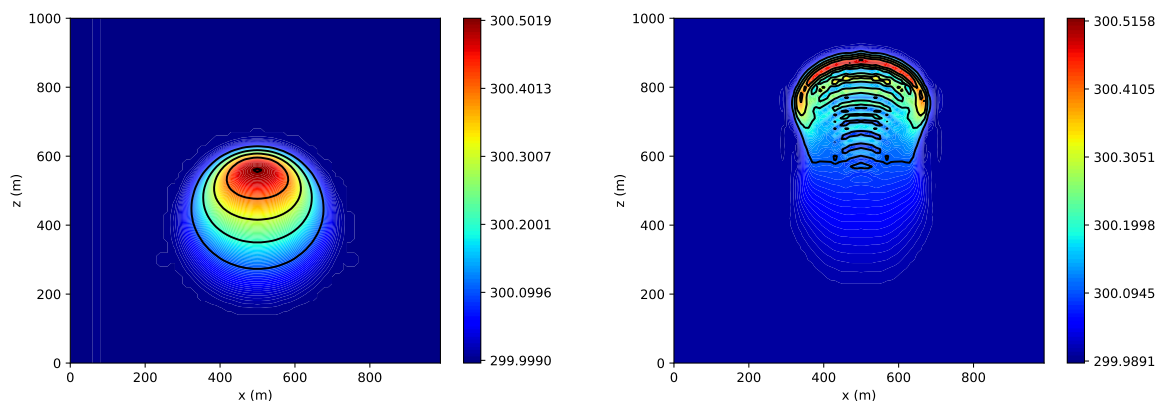


Figure 8: Potential temperature cross section at $y = 0$ for the 3D rising bubble test case at times 200s (left) and 400s (right).

While the results qualitatively match those previously published in terms of both the position and deformation of the bubble [24, 25], a secondary oscillation develops in the wake of the bubble as it steepens, as shown in fig. 8. This is on account of the fact that no upwinding or dissipation is applied to the potential temperature equation. The evolution of the energy and power exchanges are shown in fig 9. These match closely with previous results using a variation on the more common TRAP(2,3,2) HEVI scheme [9], and clearly show the signature of the high frequency internal gravity wave, as well as the increase in vertical kinetic energy and decrease in potential energy which represent the ascension of the bubble.

5.2.1. Upwinding of potential temperature

In order to suppress the spurious potential temperature oscillations observed in fig. 8 in an energetically consistent manner, the upwinding formulation presented in section 4 is applied to the rising bubble test case. As observed in fig. 10, this upwinding formulation effectively clears up the spurious overshoots and oscillations. Since the upwinding is performed within the skew-symmetric operator, as detailed in (22), the energy conservation errors are almost identical to those for the original formulation, as shown in fig. 11. Note that in each case a biharmonic viscosity is applied to the horizontal momentum equation, to account for the temporal inconsistency in the energetics due to the explicit form of the horizontal time stepping, so exact energy conservation is not expected.

6. Conclusions

A new horizontally explicit/vertically implicit time splitting scheme for non-hydrostatic atmospheric dynamics is introduced. The scheme allows for the exact balance of energetic exchanges when coupled with a spatial and vertical time integration scheme that preserve the skew-symmetric property of the Hamiltonian formulation of the equations of motion. However since the choice of horizontal velocity for which exchanges balance differs from the horizontal velocity at the end of the time step, the scheme still permits an energy conservation error. Linear

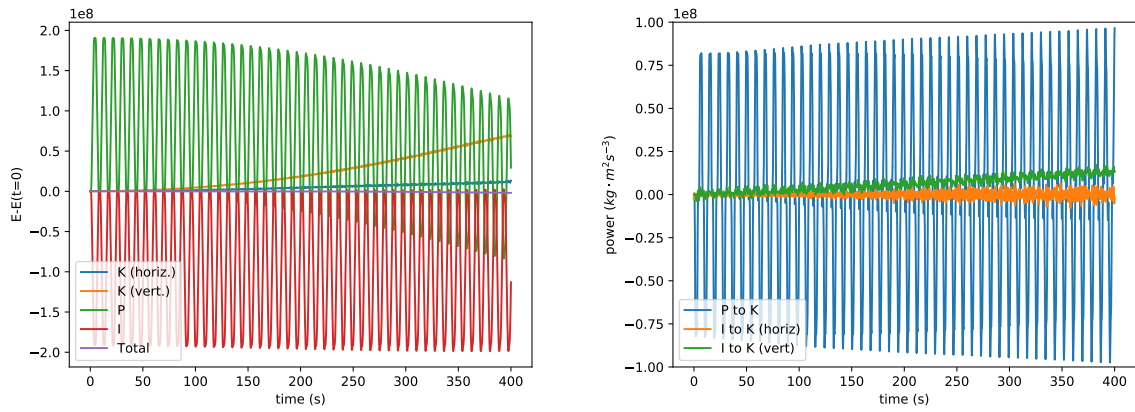


Figure 9: Difference in energy from initial value (left), and power exchanges (right) for the 3D rising bubble test case.

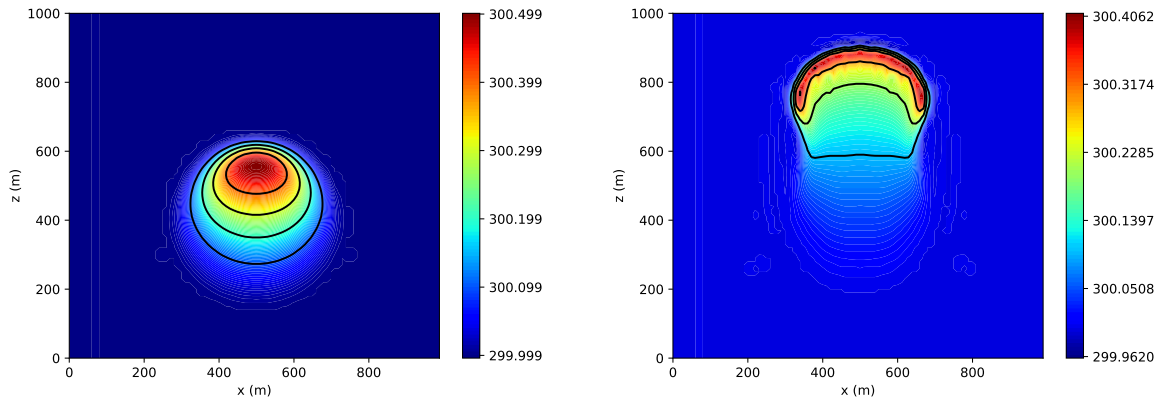


Figure 10: Upwinded potential temperature cross section at $y = 0$ for the 3D rising bubble test case at times 200s (left) and 400s (right).

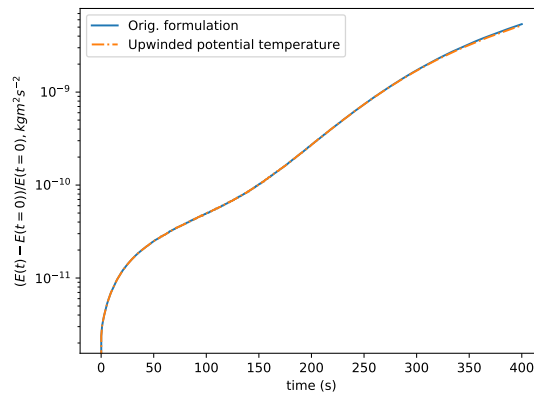


Figure 11: Comparison of energy conservation errors for the original and upwinded potential temperature formulations.

eigenvalue analysis shows that the second order scheme improves upon the existing second order trapezoidal HEVI splitting by ensuring the neutral stability of all buoyancy modes, and all acoustic modes below a certain horizontal CFL number. Comparison to a horizontally third order, vertically second order trapezoidal splitting for the full 3D compressible Euler equations on the sphere shows that both schemes exhibit a secondary oscillation in the potential to kinetic power exchanges, associated with an internal gravity mode, however this oscillation has a temporal frequency approximately four times faster for the new energetically balanced scheme, meaning this mode is less likely to alias onto the baroclinic time scales than in the traditional scheme.

An energetically consistent formulation for potential temperature upwinding is also presented, by which the test functions are evaluated at vertically downstream locations. This ensures that spurious oscillations in potential temperature can be removed for vertical motions at non-hydrostatic regimes. This upwinding is applied within the skew-symmetric formulation, so as to suppress oscillations associated with vertical motions without altering the energetic properties of the model, for which the exchanges remain balanced.

Appendix: Entropy conservation for the variational form of the compressible Euler equations

The entropy for the compressible Euler equations is defined as:

$$s = c_p \log(\theta) + s_0, \quad (39)$$

where θ is the potential temperature. The time derivative of the internal energy is derived by multiplying the density-weighted potential temperature advection equation,

$$\frac{\partial \rho \theta}{\partial t} + \nabla \cdot (\rho \mathbf{u} \theta) = 0, \quad (40)$$

by the Exner pressure,

$$\frac{\delta I}{\delta \Theta} = \Pi = c_p \left(\frac{R \rho \theta}{p_0} \right)^{R/c_v}, \quad (41)$$

such that the internal energy, I evolves as

$$\frac{\partial I}{\partial t} = \left\langle \frac{\delta I}{\delta \Theta}, \frac{\partial \Theta}{\partial t} \right\rangle = \left\langle \Pi, \frac{\partial \rho \theta}{\partial t} \right\rangle = \frac{c_v}{c_p} \frac{\partial}{\partial t} \int \rho \theta \Pi d\Omega = -\langle \Pi, \nabla \cdot (\rho \mathbf{u} \theta) \rangle, \quad (42)$$

since $R = c_p - c_v$ and $\Theta = \rho \theta$. This expression may then be expanded as:

$$\frac{c_v}{c_p} \frac{\partial}{\partial t} \int \rho \theta \Pi d\Omega = -\langle \Pi, \theta \nabla \cdot (\rho \mathbf{u}) + \rho \mathbf{u} \cdot \nabla \theta \rangle \quad (43a)$$

$$= -\left\langle \rho \theta \Pi, \frac{1}{\rho} \nabla \cdot (\rho \mathbf{u}) + \frac{\mathbf{u}}{\theta} \cdot \nabla \theta \right\rangle \quad (43b)$$

$$= \left\langle \rho \theta \Pi, \frac{\partial \log(\rho)}{\partial t} - \mathbf{u} \cdot \nabla \log(\theta) \right\rangle \quad (43c)$$

The left hand side of this expression may be re-arranged as:

$$\frac{c_v}{c_p} \int \frac{\partial \rho \theta \Pi}{\partial t} d\Omega = \frac{c_v}{c_p} \left\langle \frac{\rho \theta \Pi}{\rho \theta \Pi}, \frac{\partial \rho \theta \Pi}{\partial t} \right\rangle = \frac{c_v}{c_p} \left\langle \rho \theta \Pi, \frac{\partial \log(\rho \theta \Pi)}{\partial t} \right\rangle = \left\langle \rho \theta \Pi, \frac{\partial \log(\rho)}{\partial t} - \mathbf{u} \cdot \nabla \log(\theta) \right\rangle \quad (44)$$

For $\rho \theta \Pi \in L^2(\Omega)$, cancellation of this factor from both sides yields the variational expression

$$\frac{c_v}{c_p} \left\langle \gamma, \frac{\partial \log(\rho \theta \Pi)}{\partial t} \right\rangle = \left\langle \gamma, \frac{\partial \log(\rho)}{\partial t} - \mathbf{u} \cdot \nabla \log(\theta) \right\rangle \quad \forall \gamma \in L^2(\Omega) \quad (45)$$

Recalling the equation of state gives

$$\rho\theta\Pi = c_p \left(\frac{R}{p_0} \right)^{R/c_v} (\rho\theta)^{c_p/c_v}, \quad (46)$$

$$\left\langle \gamma, \frac{\partial \log(\rho\theta)}{\partial t} \right\rangle = \left\langle \gamma, \frac{\partial \log(\rho)}{\partial t} - \mathbf{u} \cdot \nabla \log(\theta) \right\rangle \quad \forall \gamma \in L^2(\Omega) \quad (47)$$

which is further simplified as:

$$\left\langle \gamma, \frac{\partial \log(\theta)}{\partial t} + \mathbf{u} \cdot \nabla \log(\theta) \right\rangle = 0 \quad \forall \gamma \in L^2(\Omega) \quad (48)$$

Recalling the original definition of the entropy then gives

$$\left\langle \gamma, \frac{\partial s}{\partial t} + \mathbf{u} \cdot \nabla s \right\rangle = 0 \quad \forall \gamma \in L^2(\Omega) \quad (49)$$

such that entropy is materially conserved. Setting the test function as the density $\gamma = \rho$ in the above expression, and multiplying the continuity equation by the entropy, we have

$$\left\langle \rho, \frac{\partial s}{\partial t} + \mathbf{u} \cdot \nabla s \right\rangle = 0 \quad (50a)$$

$$\left\langle s, \frac{\partial \rho}{\partial t} + \nabla \cdot \mathbf{u}\rho \right\rangle = 0 \quad (50b)$$

Adding the above expressions gives

$$\int \frac{\partial \rho s}{\partial t} + \nabla \cdot (\mathbf{u}\rho s) d\Omega = 0 \quad (51)$$

Which gives an additional conservation law for the entropy function-entropy flux pair $\rho s, \mathbf{u}\rho s$ [26].

References

- [1] P. Ullrich, C. Jablonowski, Operator-split Runge–Kutta–Rosenbrock methods for nonhydrostatic atmospheric models, *Mon. Wea. Rev.* 140 (2012) 1257–1284.
- [2] F. X. Giraldo, J. F. Kelly, E. M. Constantinescu, Implicit-explicit formulations of a three-dimensional nonhydrostatic unified model of the atmosphere (NUMA), *SIAM J. Sci. Comput.* 35 (2013) B1162–B1194.
- [3] L. Bao, R. Klöforn, R. D. Nair, Horizontally explicit and vertically implicit (HEVI) time discretization scheme for a discontinuous Galerkin nonhydrostatic model, *Mon. Wea. Rev.* 143 (2015) 972–990.
- [4] D. J. Gardner, J. E. Guerra, F. P. Hamon, D. R. Reynolds, P. A. Ullrich, C. S. Woodward, Implicit-explicit (IMEX) Runge-Kutta methods for non-hydrostatic atmospheric models, *Geosci. Model Dev.* 11 (2018) 1497–1515.
- [5] A. Steyer, C. J. Vogl, M. Taylor, O. Guba, Efficient IMEX Runge-Kutta Methods for Nonhydrostatic dynamics, arXiv:1906.07219 (2019)
- [6] H. Weller, S. J. Lock, N. Wood, Runge–Kutta IMEX schemes for the Horizontally Explicit/Vertically Implicit (HEVI) solution of the wave equations, *J. Comp. Phys.* 252 (2013) 365–381.
- [7] S.-J. Lock, N. Wood, H. Weller, Numerical analyses of Runge–Kutta implicit–explicit schemes for horizontally explicit, vertically implicit solutions of atmospheric models, *Q. J. R. Meteorol. Soc.* 140 (2014) 1654–1669.
- [8] D. Lee, A. Palha, A mixed mimetic spectral element model of the 3D compressible Euler equations on the cubed sphere, *J. Comp. Phys.* 401 (2020) 108993.
- [9] D. Lee, An energetically balanced, quasi-Newton integrator for non-hydrostatic vertical atmospheric dynamics, *J. Comp. Phys.* 426 (2021) 109988.
- [10] D. Lee, A. Palha, M. Gerritsma, Discrete conservation properties for shallow water flows using mixed mimetic spectral elements, *J. Comp. Phys.* 357 (2018) 282–304.
- [11] D. Lee, A. Palha, A mixed mimetic spectral element model of the rotating shallow water equations on the cubed sphere, *J. Comp. Phys.* 375 (2018) 240–262.
- [12] M. Gerritsma, Edge functions for spectral element methods, in: *Spectral and high order methods for partial differential equations*, Lecture Notes in Computational Science and Engineering, Springer 76 (2011) 199–207.
- [13] J. Kreeft, M. Gerritsma, Mixed mimetic spectral element method for Stokes flow: A pointwise divergence-free solution, *J. Comp. Phys.* 240 (2013) 284–309.

- [14] A. Palha, P. P. Rebelo, R. Hiemstra, J. Kreeft, M. Gerritsma, Physics-compatible discretization techniques on single and dual grids, with application to the Poisson equation of volume forms, *J. Comp. Phys.* 257 (2014) 1394–1422.
- [15] R. Hiemstra, D. Toshniwal, R. H. M. Huijsmans, M. I. Gerritsma, High order geometric methods with exact conservation properties, *J. Comp. Phys.* 257 (2014) 1444–1471.
- [16] M. Gerritsma, P. Bochev, A spectral mimetic least-squares method for the Stokes equations with no-slip boundary conditions, *Comput. Math. Appl.* 71 (2016) 2285–2300.
- [17] D. Durran, *Numerical Methods for Fluid Dynamics: With Applications in Geophysics*, Springer (2010) 516pp.
- [18] R. Sadourny, C. Basdevant, Parameterization of Subgrid Scale Barotropic and Baroclinic Eddies in Quasi-geostrophic Models: Anticipated Potential Vorticity Method, *J. Atmos. Sci.* 42 (1985) 1353–1363
- [19] A. T. T. McRae, C. J. Cotter, Energy- and enstrophy conserving schemes for the shallow water equations, based on mimetic finite elements, *Q. J. R. Meteorol. Soc.* 140 (2014) 2223–2234.
- [20] D. Lee, Petrov-Galerkin flux upwinding for mixed mimetic spectral elements, and its application to geophysical flow problems, *arXiv:2004.13225* (2020)
- [21] G. A. Wimmer, C.J. Cotter, W. Bauer, Energy conserving SUPG methods for compatible finite element schemes in numerical weather prediction, *arXiv:2001.09590* (2020)
- [22] A. N. Brooks, T. J. R. Hughes, Streamline upwind/Petrov-Galerkin formulations for convection dominated flows with particular emphasis on the incompressible Navier-Stokes equations, *Comput. Meth. Appl. Mech. Engrg.* 32 (1982) 199–259
- [23] P. A. Ullrich, T. Melvin, C. Jablonowski, A. Staniforth, A proposed baroclinic wave test case for deep- and shallow-atmosphere dynamical cores, *Q. J. R. Meteorol. Soc.* 140 (2014) 1590–1602.
- [24] D. S. Abdi, F. X. Giraldo, Efficient construction of unified continuous and discontinuous Galerkin formulations for the 3D Euler equations, *J. Comp. Phys.* 320 (2016) 46–68.
- [25] T. Melvin, T. Benacchio, B. Shipway, N. Wood, J. Thuburn, C. Cotter, A mixed finite-element, finite-volume, semi-implicit discretisation for atmospheric dynamics: Cartesian geometry, *Q. J. R. Meteorol. Soc.* (2019) 1–19.
- [26] E. Tadmor, Entropy stability theory for difference approximations of nonlinear conservation laws and related time-dependent problems, *Acta Numerica* 12 (2003) 451–512.